

SYSTEMATIC UNCERTAINTIES IN THE SPECTROSCOPIC MEASUREMENTS OF NEUTRON-STAR MASSES AND RADII FROM THERMONUCLEAR X-RAY BURSTS. III. ABSOLUTE FLUX CALIBRATION

TOLGA GÜVER^{1,2}, FERYAL ÖZEL³, HERMAN MARSHALL⁴, DIMITRIOS PSALTIS³, MATTEO GUAINAZZI⁵, & MARIA DÍAZ-TRIGO⁶

¹ Istanbul University, Science Faculty, Department of Astronomy and Space Sciences, Beyazıt, 34119, Istanbul, Turkey

² Istanbul University Observatory Research and Application Center, Beyazıt, 34119, Istanbul, Turkey

³ Department of Astronomy, University of Arizona, 933 N. Cherry Ave., Tucson, AZ 85721

⁴ Center for Space Research, Massachusetts Institute of Technology, Cambridge, MA 02139

⁵ European Space Astronomy Centre of ESA, PO Box 78, Villanueva de la Cañada, E-28691 Madrid, Spain and

⁶ ESO, Karl-Schwarzschild-Strasse 2, D-85748 Garching bei München, Germany

Draft version September 3, 2018

ABSTRACT

Many techniques for measuring neutron star radii rely on absolute flux measurements in the X-rays. As a result, one of the fundamental uncertainties in these spectroscopic measurements arises from the absolute flux calibrations of the detectors being used. Using the stable X-ray burster, GS 1826–238, and its simultaneous observations by Chandra HETG/ACIS-S and RXTE/PCA as well as by XMM-Newton EPIC-pn and RXTE/PCA, we quantify the degree of uncertainty in the flux calibration by assessing the differences between the measured fluxes during bursts. We find that the RXTE/PCA and the Chandra gratings measurements agree with each other within their formal uncertainties, increasing our confidence in these flux measurements. In contrast, XMM-Newton EPIC-pn measures $14.0 \pm 0.3\%$ less flux than the RXTE/PCA. This is consistent with the previously reported discrepancy with the flux measurements of EPIC-pn, compared to EPIC-MOS1, MOS2 and ACIS-S detectors. We also show that any intrinsic time dependent systematic uncertainty that may exist in the calibration of the satellites has already been implicitly taken into account in the neutron star radius measurements.

Subject headings: stars: neutron — X-rays: bursts

1. INTRODUCTION

Measurements of the masses and radii of neutron stars provide unique information on the equation of state of matter at densities above the nuclear saturation density. Extremely accurate mass measurements in binary systems can be obtained through dynamical methods (see, e.g., Stairs 2006; Demorest et al. 2010). However, without independent determinations of the radii of these neutron stars, these measurements provide only limits for the equation of state. In contrast, an accurate measurement of the radius of even a single neutron star can provide strong constraints on the equation of state of neutron star matter (Lattimer & Prakash 2001; Özel & Psaltis 2009; Read et al. 2009).

Thermonuclear X-ray bursts observed from low mass X-ray binaries have proven to be one of the most suitable events that can be used to measure both the radii and the masses of neutron stars (see, e.g., van Paradijs 1978, 1979; Damen et al. 1990; Lewin, van Paradijs, & Taam 1993; Özel 2006). Using high signal-to-noise X-ray data and time-resolved spectroscopy allows a measurement of the apparent radius during the cooling segments of the bursts. In addition, time-resolved spectroscopy during a photospheric radius expansion burst enables a measurement of the Eddington luminosity for each source. Combining these two measurements leads to an uncorrelated determination of the neutron star mass and radius.

Thanks to the Rossi X-ray Timing Explorer (RXTE), which provided more than 15 years of observations of bursts (Galloway et al. 2008), it has now become possible to not only make neutron star mass and radius measurements using observations of specific systems (see, e.g., Özel, Güver, & Psaltis 2009) but also to quantify the systematic uncertainties in these measurements. In Paper I of these series (Güver, Psaltis, & Özel 2012a), we analyzed more than 13,000 X-ray spectra from 12 different sources and showed that the errors in the spectroscopic determination of neutron-star radii due to systematic effects in the cooling tails of X-ray bursts are in the range of $\simeq 3\%–8\%$. In Paper II (Güver, Özel, & Psaltis 2012b), we used all the archival photospheric radius expansion bursts and found that for sources from which a large number of bursts are observed, systematic uncertainties in the determination of the Eddington flux are at the 5%–10% level.

In this paper, we focus on a third possible source of systematic uncertainty, which is the absolute flux calibration of the Proportional Counter Array (PCA) on board RXTE. Absolute flux uncertainties affect the normalization of the spectra obtained during bursts and therefore the measurement of both the apparent radii and of the Eddington flux.

Determining the absolute flux calibration of an X-ray detector requires a major effort from any instrument team and all X-ray observatories put large amount of resources into in-flight calibrations of their detectors. However, these efforts are hindered by the fact that almost all X-ray sources in the sky that may be used as standard candles often show unpredicted variability over both long and short time scales (see, e.g., Wilson-Hodge et al. 2011, and references therein for the recent activity of the Crab Nebula). Additionally, complications due to significantly different responses

of different detectors, both in terms of effective areas and the energy ranges that the detectors are sensitive to, become a major hurdle and restrict the inter-calibration efforts. Furthermore, the often unknown intrinsic spectral shape of the astronomical objects being used for the calibration makes the problem even more complex. Simultaneous observations of sources with well known intrinsic spectra by two or more X-ray detectors that have different energy responses allow us to better understand and quantify the systematic uncertainties in the absolute flux calibrations of individual detectors.

In the early days of high energy astrophysics, the Crab Nebula was seen as the ideal stellar source for the calibration of various instruments. Compiling a number of rocket, balloon, and satellite observations performed between 1964 and 1972, Toor & Seward (1974) concluded that the diffuse X-ray emission should be steady at least for the time period they analyzed, since any variation in the pulsar emission larger than 10% at a few keV would have been detected. With these limits, they assumed that the Crab is a steady source and provided a “universal” power-law amplitude and photon-index with their relevant uncertainties. In the following years, these values were often cited and used as a reference point to calibrate the performance of various instruments. Norgaard-Nielsen et al. (1994) even proposed a specific mission called *eXCALIBur* to continuously monitor the Crab Nebula using two pinhole cameras one with a CCD and another with a proportional counter to measure the spectrum of the nebula with an accuracy $<2\%$ over the energy range 0.8–20 keV. Such a mission could, in principle, be a reliable inter-calibration reference for subsequent detectors.

Using the Crab as a standard source, Kirsch et al. (2005) compared the XMM-Newton/EPIC-pn measurements of the spectrum of Crab with those from all the other modern X-ray satellites. In particular, they found that although the photon index inferred from XMM-Newton/EPIC agrees within errors with the Toor & Seward (1974) value, the normalization derived from EPIC-pn is significantly lower than that from the rest of the instruments. They also noted that, with the new generation of instruments, Crab is becoming a source that is too bright and too extended to be used as a standard calibration source. In a similar, later study, Weisskopf et al. (2010) investigated possible departures from a single power-law of the intrinsic spectrum of Crab for ROSAT/PSPC, RXTE/PCA, and the XMM-Newton/EPIC-pn, which would affect the instrument calibrations. Using the high statistical quality of the RXTE/PCA data, these authors concluded that they would have been able to detect significant deviations from a simple power-law spectrum but they did not find any evidence for such a deviation.

With the advancement of imaging detectors and considering the brightness of the Crab for the onboard CCDs, searches for new calibration sources and techniques started. In order to coordinate and improve the efforts on inter-calibration, a group of instrument teams formed The International Astronomical Consortium for High-Energy Calibration (IACHEC, Sembay et al. 2010). One of the recent results of this group demonstrates that in the 2.0–7.0 keV range, EPIC-pn measures systematically lower fluxes than the Chandra ACIS, by $11.0\pm 0.5\%$ (Nevalainen et al. 2010), using a sample of 11 nearby clusters of galaxies. The difference is smaller yet still significant when ACIS is compared with EPIC MOS1 and MOS2, with differences at $3.0\pm 0.5\%$ and $6.0\pm 0.5\%$, respectively (Nevalainen et al. 2010).

The spectroscopic measurements of neutron star masses and radii have been predominantly performed with RXTE. Launched in 1995 and operated until 2012, RXTE/PCA has always been calibrated against the Crab Nebula (Jahoda et al. 2006; Shaposnikov et al. 2012) together with an onboard calibration source used mainly for channel-to-energy conversion. Throughout the mission, any possible variations in the Crab, as the one reported by Wilson-Hodge et al. (2011), were assumed to be averaged out (Shaposnikov et al. 2012); this issue will be discussed further in Section 5. Because the PCA was intrinsically calibrated against the Crab and because it is a non-imaging instrument, inter-calibration of the PCA has always been a challenge, especially as more and more sources such as clusters of Galaxies or similarly soft and relatively dim objects (i.e., RX J1856.5–3754) started to be used as standard candles.

Time resolved X-ray spectra extracted during thermonuclear X-ray bursts observed from low mass X-ray binaries offer a different opportunity in determining the systematic uncertainties caused by calibrations of different detectors. Since the early studies of X-ray bursts, it has been shown that the burst X-ray spectra can statistically be modeled with blackbody functions (see, e.g., Swank et al. 1977; Lewin, van Paradijs, & Taam 1993; Galloway et al. 2008). In Paper I, we analyzed more than 13,000 X-ray spectra extracted from the cooling tails of X-ray bursts observed from 12 different sources and showed that a Planckian function can statistically fit the vast majority of the observations. The high count rates of RXTE and the large number of bursts allowed us to show that any deviation from a Planckian spectrum is limited to $\leq 5\%$ in the 2.5–25.0 keV range. This almost unique characteristic of burst spectra make them ideal for testing our ability to convert countrate spectra to bolometric fluxes. Furthermore, because the obtained spectral parameters are directly related to neutron star mass-radius measurements, results obtained from an analysis of X-ray burst data can be directly converted to uncertainties in the measurements of neutron star masses and radii.

Using simultaneous RXTE, Chandra X-ray Observatory (Chandra), and XMM-Newton observations of X-ray bursts from GS 1826–238, we quantify the differences in the measurements of the apparent surface area of the thermal emission when using different detectors with independent calibrations. We describe our method in Section 2, which is based on predicting the observed Chandra and XMM-Newton countrates using time resolved spectral parameters obtained from RXTE/PCA. Section 3 details the analysis of the data from different X-ray satellites. Finally, in Sections 4 and 5 we present our results and discuss their implications.

2. METHODOLOGY

The rapid evolution of the effective temperature during the cooling tails of thermonuclear X-ray bursts demands very short exposure time observations for direct comparison of spectral data that are obtained simultaneously. The short exposures require very high countrates and, hence, detectors with large photon collecting areas. This has been

a unique property of RXTE/PCA but cannot be achieved by the other instruments that we are going to compare its results against. Therefore, we formulated an approach that does not rely on directly comparing the extracted spectra of X-ray bursts simultaneously observed with two (or more) X-ray satellites. Instead, we first analyze the RXTE data by performing time resolved X-ray spectroscopy. We extract spectra for short intervals (0.25–2.0 s depending on the countrate) and fit these data with blackbody functions. Based on the obtained χ^2 values, we then calculate the likelihood for a wide range of spectral parameters that cover the $\pm 5\text{-}\sigma$ range of the best fit values. We use this range of individual parameter pairs (blackbody temperature and normalization) to create simulations of Chandra or XMM-*Newton* X-ray spectra and then to calculate the total RXTE-predicted countrate in a given energy range. We calculate the uncertainty in these countrates by taking into account the posterior likelihoods of the RXTE/PCA parameters for each simulation. Finally, we compare this predicted countrate with the countrate actually observed by Chandra or XMM-*Newton* in the same energy range, taking into account all the associated uncertainties.

Assuming that there are no calibration uncertainties, the Chandra and/or XMM-*Newton* count rates that were predicted by analysing the RXTE observation should be in perfect agreement with the actual count rates observed with these satellites. A systematic offset on the other hand, would imply a discrepancy in the overall calibration of either or both detectors.

It is evident that this method allows for the detection of a systematic uncertainty caused by the overall flux calibration of detectors and specifically in the determination of the normalization in a particular energy range. However, the method does not allow us to constrain any calibrational uncertainties in the determination of the spectral shape.

We searched the archival RXTE observations to find the best source that can be used for this purpose. An ideal source should be a frequent burster with a number of simultaneous observations and predictable burst properties. Two low mass X-ray binaries in the archive conform to these conditions: the so-called clockwork burster GS 1826–238 and 4U 1636–536. The problem with the latter source is that its bursts do not last long enough (only about 20 s on average) to obtain sufficient amount of data to infer any systematic trends during the cooling tails of X-ray bursts. On the other hand, with bursts that last on average 130 s, GS 1826–238 provides a significant amount of counts to be used for this purpose.

2.1. GS 1826–238

GS 1826–238 was first discovered with the Ginga satellite (Makino et al. 1988; Tanaka 1989). First conclusive detections of thermonuclear X-ray bursts from this source came from BeppoSAX observations (Ubertini et al. 1997), although X-ray bursts may have been observed from this source earlier by OSO 7 (Markert et al. 1977) and OSO 8 (Becker et al. 1976). Using 2.5 years of monitoring observations by BeppoSAX, during which 70 X-ray bursts were detected, Ubertini et al. (1999) reported that the X-ray bursts show a quasi-periodicity of 5.76 hr, a remarkable characteristic of this source. Later, using 260 X-ray bursts observed with the Wide Field Camera (WFC) on board BeppoSAX over 6 years, Cornelisse et al. (2003) showed that the burst recurrence time is indeed stable but decreases as the persistent flux increases.

A total of 40 X-ray bursts were observed with the RXTE between 1997–2003 (Galloway et al. 2008). During this time interval, the persistent flux steadily increased as the burst recurrence time decreased (Galloway et al. 2008). Another remarkable feature of the X-ray bursts observed from this source is their similarity. Although the initial decay time-scale and the burst fluence show slight variations with persistent flux, the observed X-ray burst light curves are nearly identical and reproducible (Galloway et al. 2004).

The nearly identical light curves of individual bursts, predictable recurrence times, and, finally, already existing simultaneous observations with other X-ray satellites (Chandra and XMM-*Newton*) make GS 1826–238 an ideal target to understand and quantify the systematic uncertainties in the measurement of neutron-star masses and radii introduced by the uncertainties in the absolute flux calibration of RXTE/PCA.

3. DATA ANALYSIS

In this study, we use data from three different X-ray satellites. GS 1826–238 was observed simultaneously by Chandra and RXTE for the first time in 2002, where three X-ray bursts were recorded. We present the analysis of these bursts below. Furthermore, RXTE observed the system in 2003 simultaneously with XMM-*Newton*. During this observation, 7 X-ray bursts were detected with RXTE. We analyze here 5 of these events because, during one of the remaining bursts, XMM-*Newton* was affected by high energy particle background (burst #28) while the other burst was only partially observed and did not have high time resolution data with RXTE/PCA (burst #29). We present a log of these bursts in Table 1.

3.1. RXTE

The RXTE observations were analyzed following the method detailed in Paper I. Time resolved, 2.5–25.0 keV X-ray spectra were extracted from science event mode data (125 μs time resolution and 64 energy channels) using the *ftool* *seextract* from all of the RXTE/PCA layers. For each burst, spectra were integrated over 0.25, 0.5, 1 or 2 s time intervals so that the total number of counts in each spectrum remain roughly the same while the countrate decreases during a burst. A 16 s X-ray spectrum was extracted from a time interval just prior to each burst, as the spectrum of the persistent emission, and subtracted from the X-ray burst spectra as background. We took the PCA deadtime correction into account following the procedure described in Paper I.

Response matrix files were created for each burst separately using the PCARSP version 11.7, HEASOFT 6.7 and HEASARC's remote calibration database. X-ray spectral analysis was performed using the Interactive Spectral Inter-

TABLE 1
ANALYZED X-RAY BURSTS

Burst ID ^a	Start Time (MJD) ^a	RXTE Observation ID	Simultaneous Obs.
22	52484.41775	70044-01-01-000	Chandra
23	52484.56684	70044-01-01-00	Chandra
24	52485.00672	70044-01-01-02	Chandra
26	52736.53279	80048-01-01-00	XMM- <i>Newton</i>
27	52736.66488	80048-01-01-010	XMM- <i>Newton</i>
28 ^b	52736.80048	80048-01-01-010	XMM- <i>Newton</i>
29 ^c	52738.34118	80048-01-01-04	XMM- <i>Newton</i>
30	52738.47686	80048-01-01-04	XMM- <i>Newton</i>
31	52738.61013	80048-01-01-07	XMM- <i>Newton</i>
32	52738.74636	80048-01-01-07	XMM- <i>Newton</i>

^a Burst IDs and burst start times are adopted from Galloway et al. (2008).

^b This burst is excluded from further analysis because, during the burst XMM-*Newton* was exposed to high background flaring activity.

^c This burst is excluded from the analysis because it was only partly observed by the RXTE and high time resolution data modes of RXTE/PCA did not cover the burst (Galloway et al. 2008).

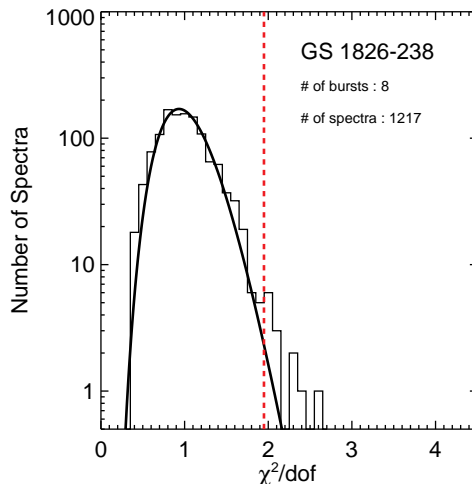


FIG. 1.— Histogram showing the χ^2/dof distribution obtained from fitting 1217 X-ray spectra extracted from 8 thermonuclear X-ray bursts observed from GS 1826–238. The solid line shows the expected χ^2/dof distribution for the number of degrees of freedom in the fits. The vertical dashed line correspond to the highest value of χ^2/dof that we considered to be statistically acceptable.

pretation System (ISIS), version 1.4.9-55 (Houck & Denicola 2000) and, for each fit, a systematic uncertainty of 0.5% was included as suggested by the RXTE calibration team¹. We note that we also investigated the possibility of photon pile-up in the RXTE/PCA data following Tomsick & Kaaret (1998)² and Jahoda et al. (2006). During the decay of the X-ray bursts investigated here, the observed count rates are ≈ 1600 cts/s/PCU, which is far below the threshold of 10000 cts/s/PCU, where pile-up can become important according to those studies. We, therefore, conclude that photon pile-up in the PCA does not affect our results.

We fit each spectrum with a blackbody function using the *bbodyrad* model (as defined in XSPEC, Arnaud 1996). Pinto et al. (2010) reported an analysis of high resolution X-ray spectroscopy of the interstellar medium toward GS 1826–238 and found an equivalent hydrogen column density of $N_{\text{H}} = 0.414 \times 10^{22} \text{ cm}^{-2}$. In order to take into account the effect of the interstellar extinction in the X-ray spectra, we used this value with the *phabs* model in XSPEC. We set the elemental abundances to the protosolar abundances of Lodders (2003), following Pinto et al. (2010). The resulting histogram of χ^2/dof values obtained from the cooling tails of all the bursts and the spectral evolution during one of the bursts (burst #23) are given in Figures 1 and 2. Similar to the results we obtained for a number of sources in Paper I, the blackbody model could adequately fit the data with a systematic uncertainty ξ of only $\approx 3\%$.

3.2. Chandra X-ray Observatory

Chandra observed GS 1826–238 in 2002 for approximately 70 ks (OBSID 2739). We analyzed the data using the *chandra_repro* tool with CIAO version 4.3 and CALDB 4.4.5. The *chandra_repro* script automates the data processing following the standard pipeline steps but applies the latest available calibrations. Using the *dmextract* tool we created a 2.5–8.0 keV range background-subtracted source lightcurve using only the data from the grating arms (+/- 1st

¹ <http://www.universe.nasa.gov/xrays/programs/rxte/pca/doc/rmf/pcarmf-11.7/>

² http://heasarc.gsfc.nasa.gov/docs/xte/pca/tomsick_98.pdf

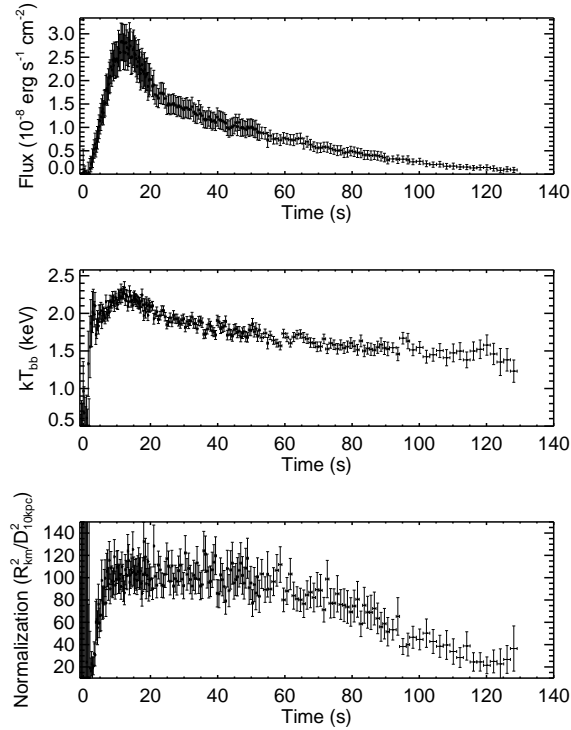


FIG. 2.— Evolution of the spectral parameters during burst #23 as observed by RXTE.

orders). The zeroth order data for this observation is saturated due to the high countrate of the source and the nominal frame time of 1.7 s.

Even for the grating arms, pile-up was significant during the peak of the bursts. In order to correctly carry out the comparison between the RXTE and Chandra observations, we opt to correct for pile-up the *predicted* Chandra countrates based on the RXTE spectra, as opposed to correcting the observed Chandra countrates. Because RXTE observations have better statistics, this forward folding of the correction does not unnecessarily inflate the uncertainties. We applied a pile-up correction procedure that is described in the Appendix, which was developed based on the understanding of the detector properties and calibrated against independent data. The evolution of the applied correction is shown in Figure 3 for burst #23. At the burst peak, photon pile-up causes a net loss of 25% of the flux, which can be recovered by the pile-up correction model that was developed independently of the present data (see the Appendix). Nevertheless, the rise and the peak of each burst, which approximately correspond to the first 30 s, are most heavily affected by pile-up. Furthermore, the rise and the peak are also the periods where the intrinsic spectrum may show some deviation from a Planckian shape; this is expected from theoretical model spectra and was discussed in Paper I using RXTE observations. Because of these reasons, we exclude the first 30 s of all Chandra bursts from our analysis such that in the time interval that we use, the pile-up fraction decreases to 2%.

We used the *mkgrmf* and *fullgrf* tools to create observation specific response and auxiliary response files for the first orders of the high energy transmission grating (HETG) and used these when creating the simulations based on the spectral parameters determined from time resolved X-ray spectroscopy.

3.3. XMM-Newton

XMM-Newton observed GS 1826–238 in 2003 for approximately 200 ks with two different back-to-back exposures that lasted 107,850 and 91,916 s (OBSIDs : 0150390101, 0150390301). The observation was performed with EPIC-pn in TIMING mode and the EPIC-MOS detectors were turned off. We analyzed the EPIC-pn data using the SAS version 11.0.0 (xmmsas.20110223.1801-11.0.0) and the calibration files as of June 2011. We calibrated the observation with the *epproc* tool. Due to the high energy particle background we could only use the first 67 ks of the first observation and ≈ 80 ks of the second. Similar to the Chandra Observation, we extracted background subtracted source light curves in the 2.5 – 10.0 keV range using the SAS tool *epicccorr*. The observatory guide² gives a limit of 450 ct/s for telemetry of the EPIC-pn timing mode, which can be increased if some of the other instruments are turned off as in this case. In the burst lightcurves that were observed with XMM-Newton, two gaps that last approximately 10 s (see Figures 7 and 8) are seen. These are most likely due to this limit. While creating the simulations we calculated observation specific effective area and redistribution matrix files using the SAS tools *rmfgen* and *arfgen*.

In order to explore the possibility of pile-up in the EPIC-pn data, we created two event lists: one including the full PSF for the source and another where the central two pixels, which should be the most affected from pile-up,

² http://xmm.esac.esa.int/external/xmm_user_support/documentation/uhb/epicmode.html

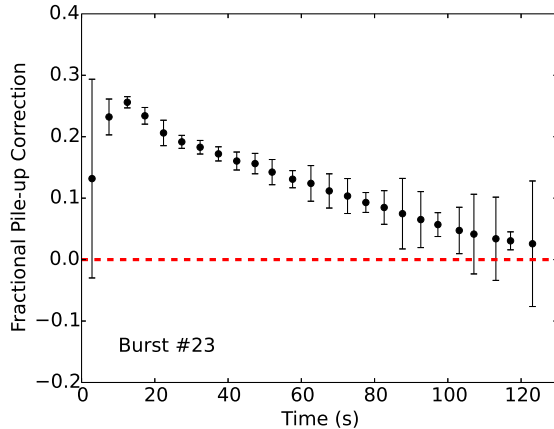


FIG. 3.— Evolution of the pile-up correction applied to the predicted Chandra countrates based on the RXTE spectra as burst #23 proceeds. For clarity the data are binned to 5 s intervals.

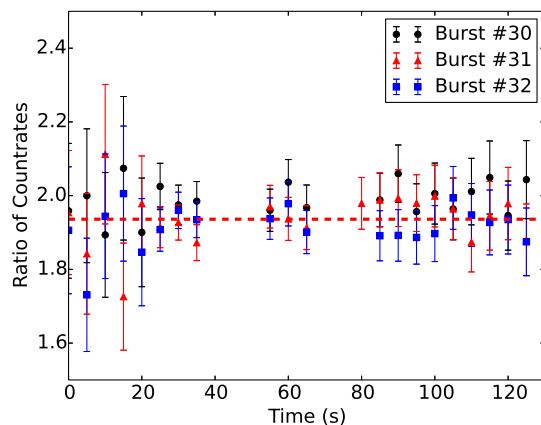


FIG. 4.— Ratio of countrates obtained when the full PSF is used to the countrates when the central two pixels are excised, for three bursts observed with XMM-Newton. For clarity the lightcurve is binned to 5 s intervals are excised. If pile-up were significant, the ratio of the countrates in the two event lists would evolve as the count rate changes during the burst because the two event lists would be subject to different amounts of pile-up. The ratio of the two lightcurves is shown in Figure 4 for bursts #30, 31, and 32. As expected, a large fraction of counts are collected in the central two pixels, making this ratio approximately equal to two. However, as the burst evolves, the ratio remains constant at the few percent level, implying that the pile-up effect will be at most of the same order. We consider this as strong evidence for the lack of any pile-up effect on the measured fluxes. Nevertheless, in order to avoid any residual effects of photon pile-up and any possible deviations from a Planckian shape, as with the Chandra bursts, we exclude the first 30 s of each burst when determining the systematic offsets between the instruments. We show these time intervals in the plots for comparison and completeness.

4. COMPARISON BETWEEN RXTE, CHANDRA, AND XMM-NEWTON

We followed the method outlined in Section 2 for comparing all of the X-ray bursts observed simultaneously with RXTE and Chandra or with RXTE and XMM-Newton. Briefly, our analysis steps are as follows:

1. We first obtained the best fit values of the parameters for each burst spectrum observed with RXTE/PCA. We then calculated the two-dimensional confidence contours for the resulting color temperature and the blackbody normalization parameters covering a $\pm 5 - \sigma$ range from the best fit values. An example confidence contour is shown in Figure 5 for the spectrum obtained approximately 9.7 s after Burst #26 started. Note that we show 68% and 95% confidence contours in the figure but use the entire likelihood in the calculations.
2. For each pair of spectral parameters, we calculated the predicted countrates for the Chandra gratings (only the ± 1 st orders for HEG and MEG) in the 2.5–8.0 keV range and for XMM-Newton/EPIC-pn countrates in the 2.5–10.0 keV range (i.e., the energy range that matches the RXTE/PCA sensitivity). For the case of the Chandra simulations, we applied the pile-up correction, as described in the previous section.
3. In order to take into account the uncertainties in the RXTE/PCA modeling, we used the posterior likelihoods over the parameters for each spectral fit to calculate the uncertainty in the total predicted countrates.

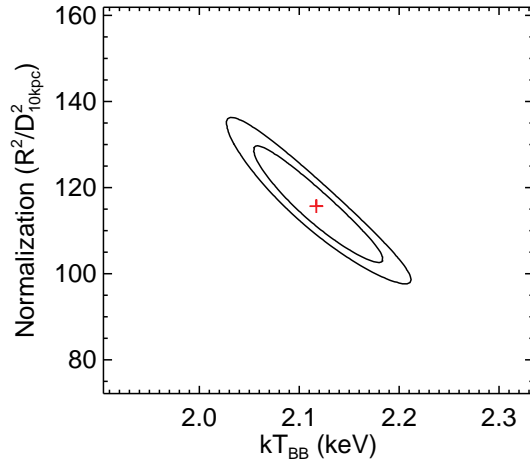


FIG. 5.— Two dimensional 68% and 95% confidence contours for the spectral parameters obtained from the fit to an X-ray spectrum extracted approximately 9.7 s after the start of burst #26. In the calculation of the uncertainty in the total predicted countrate, the whole range of parameter values are taken into account together with their posterior likelihood.

4. Finally, we compared the observed Chandra HETG/ACIS-S or XMM-*Newton*/EPIC-pn countrates to the countrates predicted using the RXTE/PCA spectral fits. For this comparison, we binned the countrates to match the time resolution of each data set and subtracted the persistent flux level of the source from the burst emission. During the Chandra observation, the nominal frame time was 1.7 s. The time resolution of the EPIC-pn observation was much higher. We, therefore, binned the EPIC-pn data to match the varying exposure time of RXTE spectra.

In Figures 6, 7, and 8, we show the time evolution of the source countrate during each X-ray burst simultaneously observed with RXTE and Chandra in the 2.5–8.0 keV range or with RXTE and XMM-*Newton* in the 2.5–10.0 keV range. In principle, all of the calculated ratios should be equal to unity within their formal uncertainties, if there are no systematic calibration differences. It is already evident from this figure that this is indeed the case between RXTE and Chandra but that there is a systematic calibration offset between RXTE and XMM-*Newton*.

To explore in more detail the calibration differences between the three instruments and whether such differences evolve with countrate, we performed two analyses. First, for the XMM-*Newton*/EPIC-pn data, for which we infer the largest systematic calibration offset, we created histograms of the ratios of the predicted and observed countrates with varying start times compared to the burst start times (see Figure 9). If there were a significant countrate dependence of the calibration offset, we would have seen a significant change in the distribution of calculated ratios at later stages of these bursts. However, it is evident from Figure 9 that there is no such time dependent change in the ratios.

Second, in order to quantify the level of offset between the three instruments, we followed the Bayesian procedure described in Papers I and II and outlined below for completeness.

We calculated the ratio f_i between the observed and predicted countrates for each time bin in the 30–120 s interval after the start of every burst together with its formal uncertainty. We assume that the uncertainty in each measurement is described by a Gaussian with a centroid $f_{0,i}$ and a dispersion σ_i i.e.,

$$P_i(f|f_{0,i}, \sigma_i) = C_i \exp \left[-\frac{(f - f_{0,i})^2}{2\sigma_i^2} \right], \quad (1)$$

where C_i is a set of normalization constants.

We will also assume that the ensemble of these ratios for each burst is drawn from a Gaussian distribution with a centroid at f_0 and a dispersion σ , i.e.,

$$P(f; f_0, \sigma) = C \exp \left[-\frac{(f - f_0)^2}{2\sigma^2} \right], \quad (2)$$

where C is a proper normalization constant. This distribution is our model for the underlying systematic flux calibration offset between the instruments. If there are no calibration differences, the centroid should be equal to one, to within σ_i/\sqrt{N} , where N is the number of measurements, and the dispersion should tend to zero. A significant offset in the flux calibration between two instruments will move f away from unity, but keep the dispersion consistent with zero. On the other hand, a large dispersion cannot be produced by an overall flux calibration offset. Instead, it likely points to effects such as an inadequate modeling of the pile-up correction, of the energy response of the detector(s), or of the astrophysical properties of the source. Our goal is to calculate the posterior likelihood for the parameters f_0 and σ , $P(f_0, \sigma|\text{data})$, given an ensemble of N measurements.

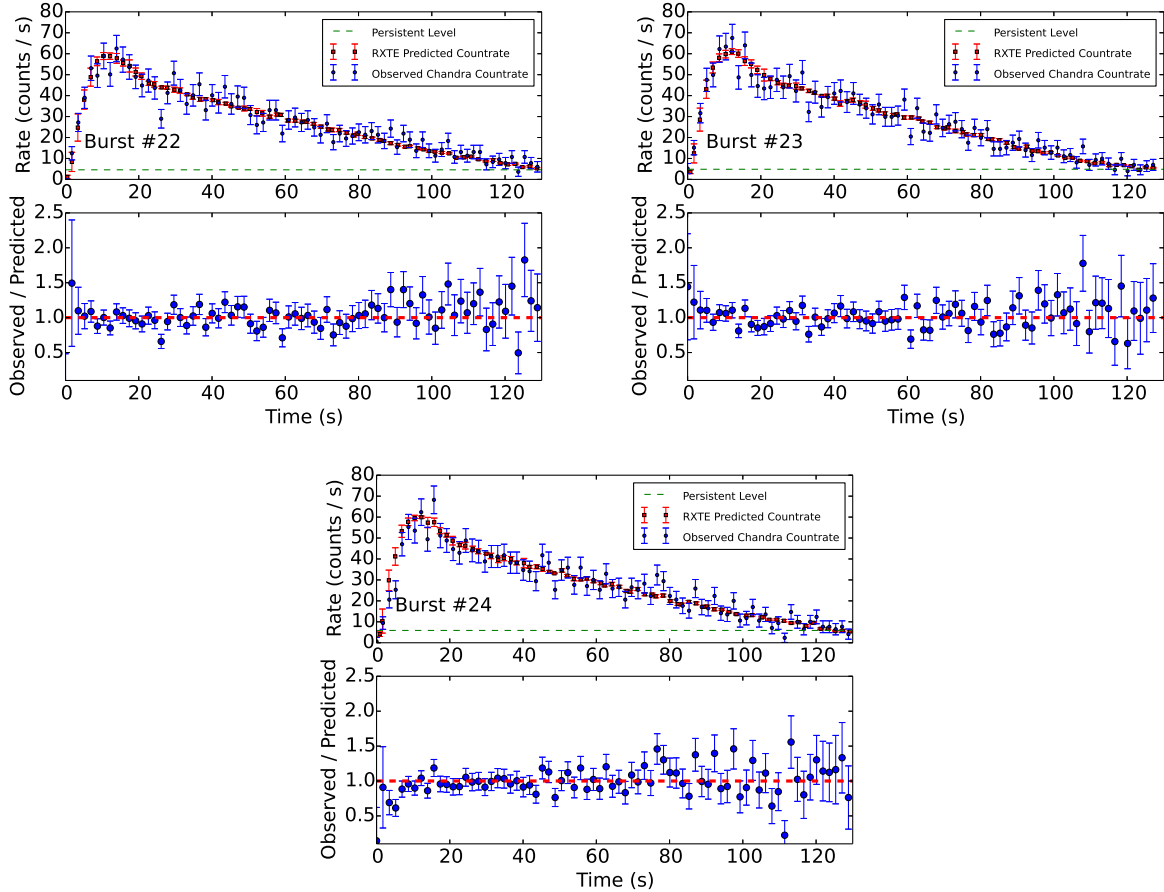


FIG. 6.— Comparison of the countrates during individual X-ray bursts as observed by Chandra HETG/ACIS and as predicted using the spectral parameters inferred during the simultaneous RXTE/PCA observations. Note that the persistent flux level of GS 1826–238 is shown with green dashed lines and it is subtracted from the observed burst lightcurve. Lower panels show the ratios of the observed and predicted countrates. The error bars in the lower panels reflect the uncertainties of both the Chandra observations and of the modeling of the RXTE observations.

Using Bayes’ theorem, we can write

$$P(f_0, \sigma | \text{data}) = C_0 P(\text{data} | f_0, \sigma) P(f_0) P(\sigma). \quad (3)$$

Here C_0 is a normalization constant, and $P(f_0)$ and $P(\sigma)$ are the priors over the centroid and dispersion of the underlying Gaussian distribution. We take these prior distributions to be flat in the range of parameters shown in Figures 10, 11, and 12, which is large enough to incorporate any range of interest. The quantity $P(\text{data} | f_0, \sigma)$ measures the likelihood that we will make a particular set of measurements given the values of the parameters of the underlying Gaussian distribution. Because these measurements are uncorrelated, we write

$$P(\text{data} | f_0, \sigma) = \prod_i \int df P_i(f | f_{0,i}, \sigma_i) P(f; f_0, \sigma). \quad (4)$$

Inserting equation (4) into equation (3) we obtain the posterior likelihood

$$P(f_0, \sigma | \text{data}) = C_0 P(f_0) P(\sigma) \prod_i \int df P_i(f | f_{0,i}, \sigma_i) P(f; f_0, \sigma), \quad (5)$$

where C_0 is an overall normalization constant. We show two-dimensional contours of these likelihoods for each burst in Figures 10, 11, and 12 and display the most likely values of the parameters in Table 2.

All figures show that the underlying distributions of offsets are extremely narrow and that the most likely values of their dispersions are consistent with being zero. This indicates that there are no systematic problems in the modeling of the energy response of the detectors and that the corrections described earlier adequately account for any pile-up effects. The most likely values of the centroids are consistent with unity for the comparison between RXTE and Chandra but as low as 0.86 for the comparison between RXTE and XMM-Newton.

Because the offsets are stable both throughout the cooling tails of individual bursts and from burst to burst, we combined all the measurements from all the bursts observed by each X-ray satellite to quantify the overall offset and

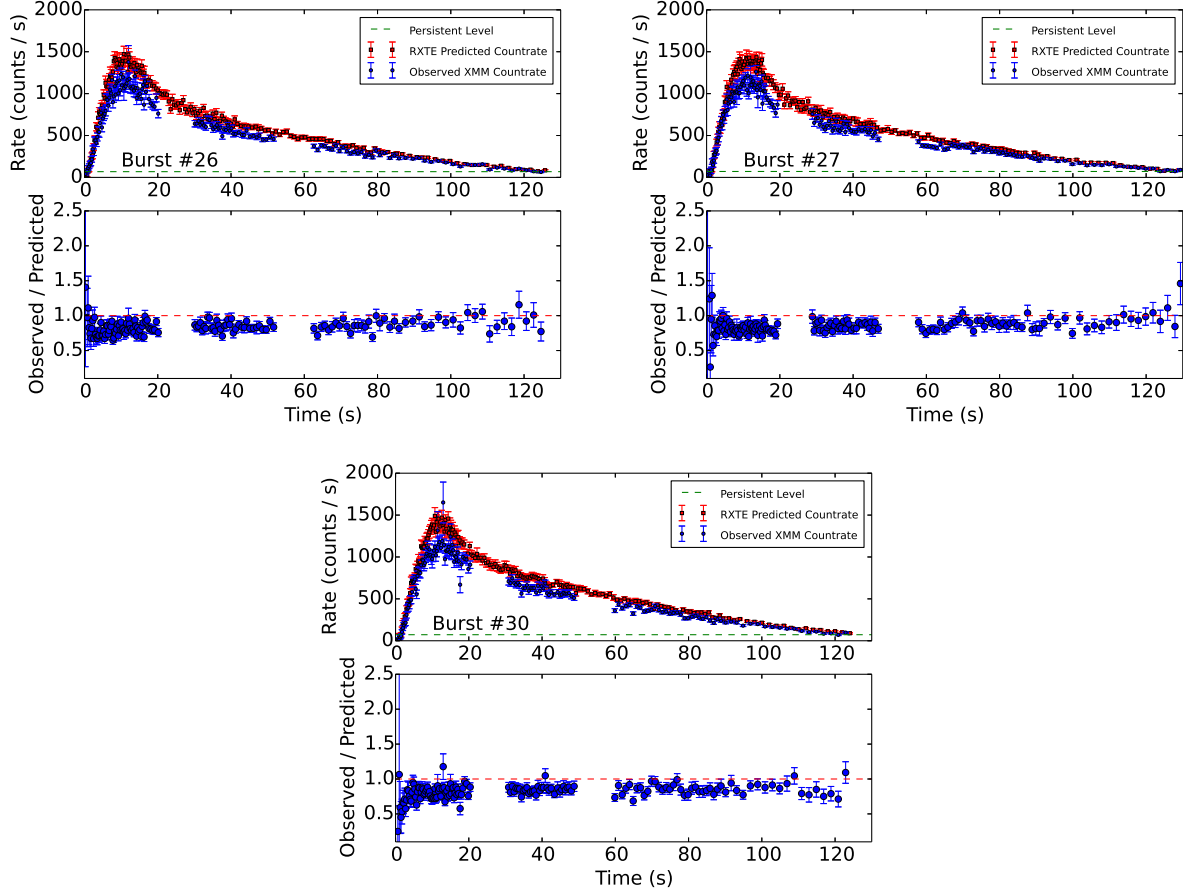


FIG. 7.— Same as Figure 6 but for the X-ray bursts #26, #27, and #30 observed simultaneously with RXTE/PCA and XMM-Newton EPIC-pn.

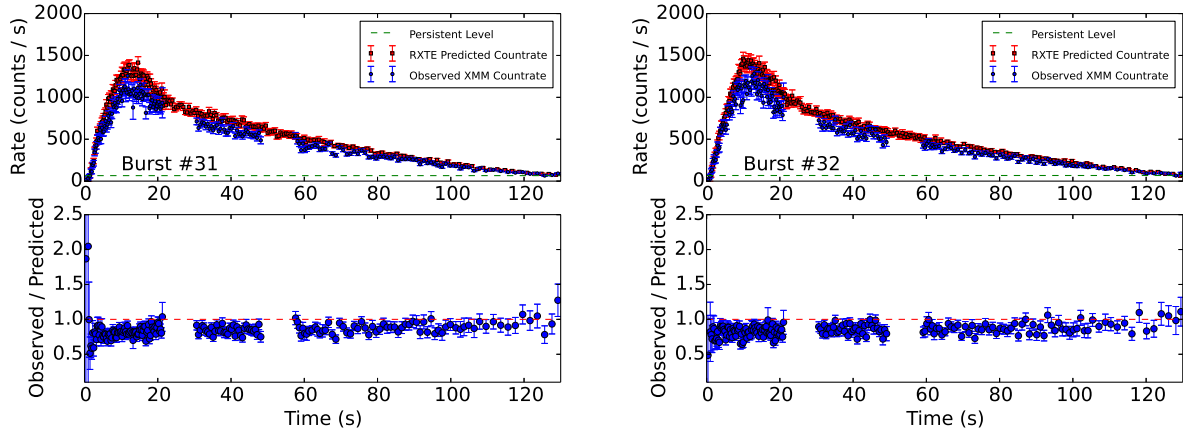


FIG. 8.— Same as Figure 6 but for the X-ray bursts #31 and #32 observed simultaneously with RXTE/PCA and XMM-Newton EPIC-pn.

its uncertainty. We computed the posterior likelihood for the offset f given the two dimensional posterior likelihood of the centroid value f_0 and dispersion σ of the underlying Gaussian distribution as

$$P(f) = \int \int P(f; f_0, \sigma) P(f_0, \sigma | \text{data}) df_0 d\sigma . \quad (6)$$

Using 5 bursts and 447 individual measurements and 3 three bursts and 170 individual measurements for comparison with XMM-Newton and Chandra, respectively, we found that the ratio of the observed count-rate with the Chandra and XMM-Newton compared to the predictions based on the RXTE spectral analysis in the 2.5 – 8.0 keV and 2.5 – 10 keV range is $1.012^{+0.006}_{-0.021}$ and 0.857 ± 0.003 , respectively. In other words, the fluxes measured with Chandra HETG/ACIS

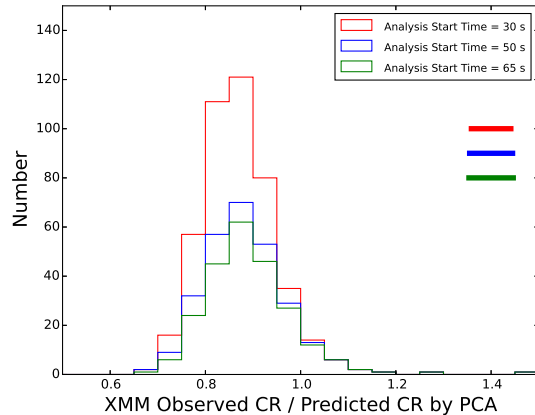


FIG. 9.— Distributions of the ratios of the predicted and observed count rates for XMM-Newton/EPIC-pn, as measured from all of the five bursts. The three histograms correspond to measurements starting at 30, 50 and 65 s after the start of each burst. The three error bars represent the average statistical errors in the measurements for each segment.

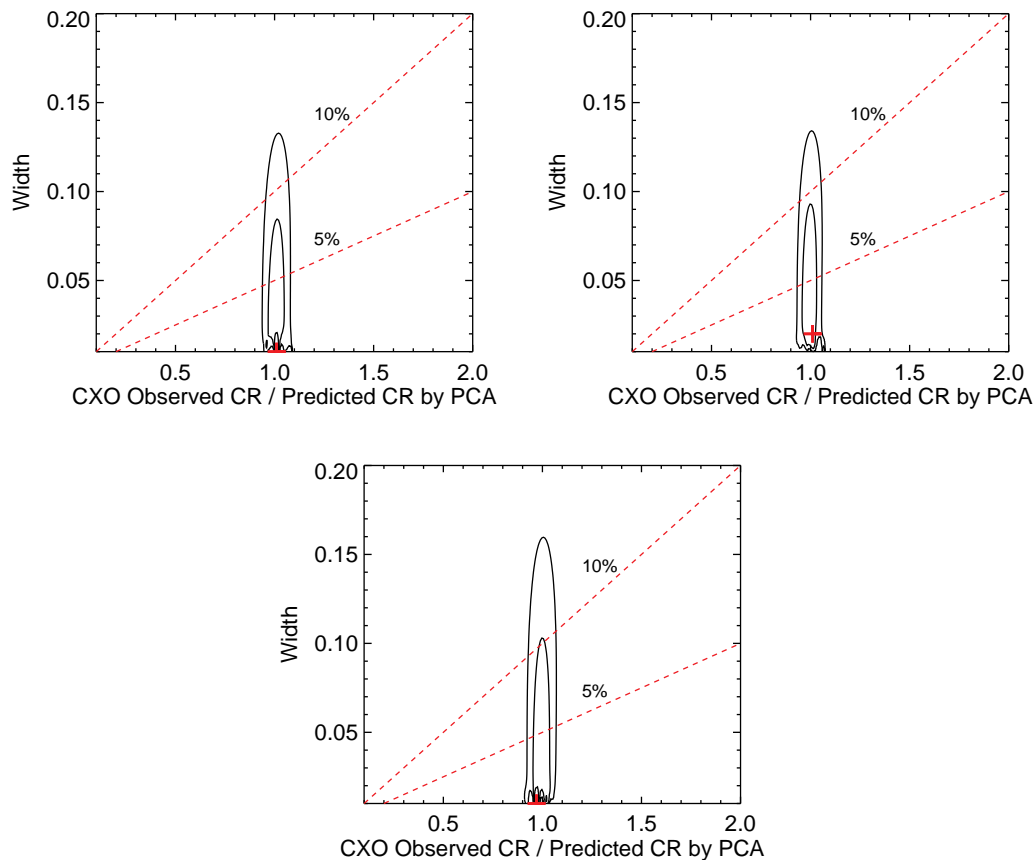


FIG. 10.— 68% and 95% confidence contours of the parameters of an assumed underlying Gaussian distribution of count-rate ratios for X-ray bursts #22, #23, and #24 observed with Chandra and RXTE simultaneously. The most likely peak of the distribution shows the offset between the satellites, while the width of the underlying distribution reflects the systematic uncertainty in the individual measurements. The dashed red lines show the width when the systematic uncertainty is 5% and 10% of the mean.

are in statistical agreement with the RXTE/PCA while the EPIC-pn measures one that is 14% less. In Figure 14, we show the combined likelihoods of the resulting ratios of count rates between the different instruments.

5. THE EFFECT OF TIME-DEPENDENT CALIBRATION

In the previous section, we addressed the cross calibration between RXTE and Chandra as well as between RXTE and XMM-Newton, using observations of the burster GS 1826–238. We obtained the most likely fractional offsets between the fluxes measured using the various instruments on simultaneous observations and showed that they are

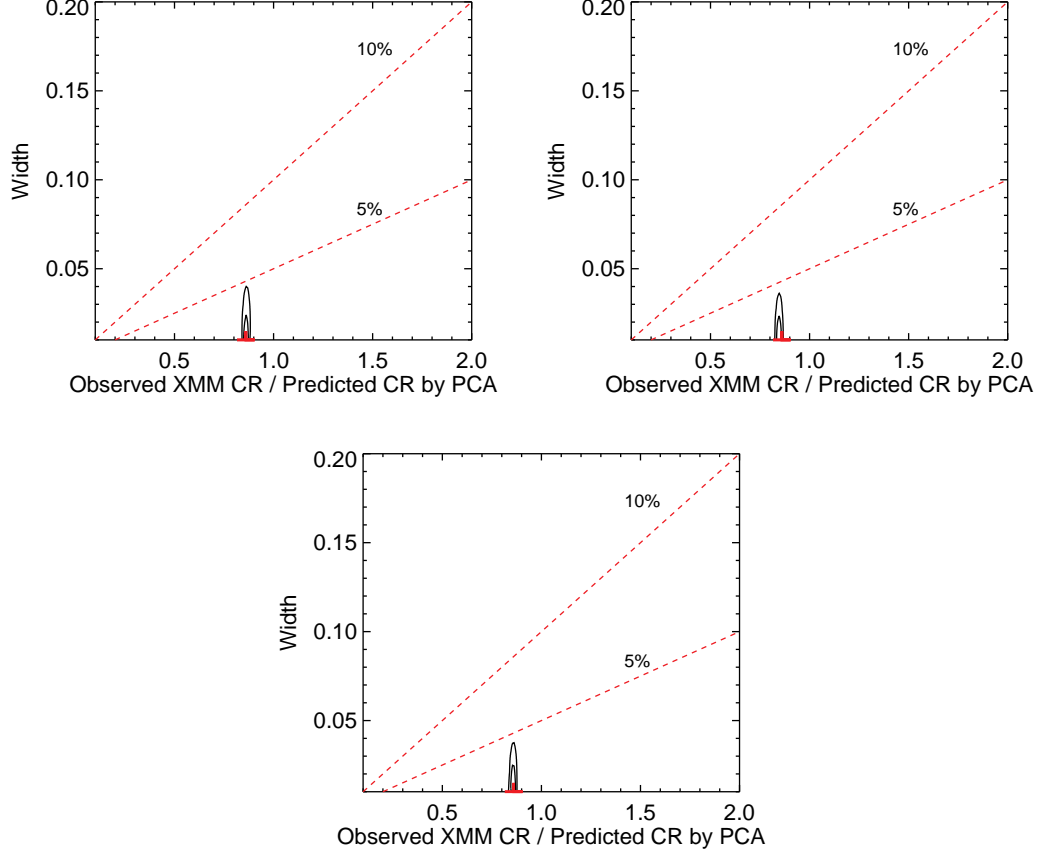


FIG. 11.— Same as Figure 10 but for bursts #26, #27, and #30 observed with XMM-Newton and RXTE simultaneously.

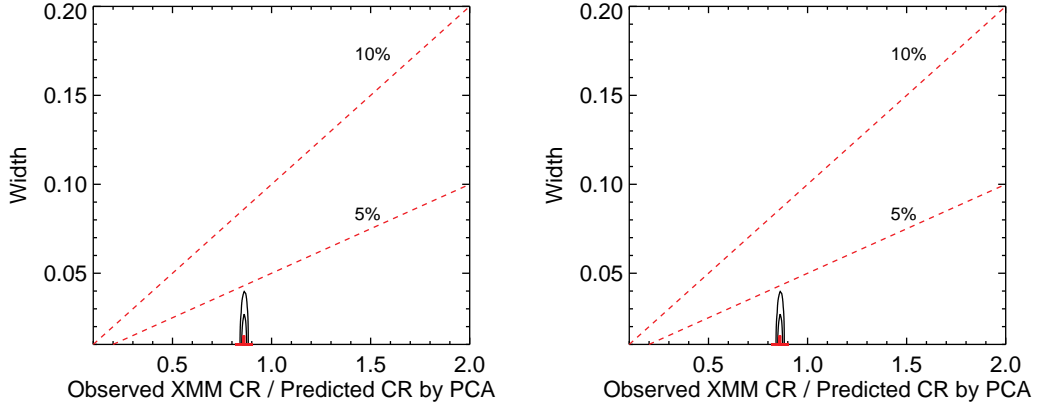


FIG. 12.— Same as Figure 10 but for bursts #31 and #32 observed with XMM-Newton and RXTE simultaneously.

consistent with being constant throughout individual bursts as well as across different bursts. However, the offsets we inferred correspond to a single point in time for each comparison.

If the efficiencies of the detectors were constant in time, the results of this comparison would be applicable to all the bursts observed throughout the durations of the missions. However, the responses of the detectors evolve with time for a number of reasons (e.g., gas leakage, charge transfer inefficiency). This evolution is typically accounted for using smooth, time-dependent models of the response parameters of the detectors. These parameters are determined by fitting the models to regular observations of the cosmic sources with known brightness and spectral shape or using internal calibrations sources (e.g. EPIC cameras). As an example, RXTE/PCA had been calibrated against the Crab nebula (Shapostnikov et al. 2013) throughout the mission.

The smooth models of the evolution of the detector response clearly cannot reliably capture the true evolution, which is expected to have a stochastic component. This will, therefore, introduce an uncertainty in the measurements that

TABLE 2
MEASURED CALIBRATION OFFSETS

Burst ID	Offset	Instruments
22	1.01	HETG-ACIS/PCA
23	1.01	HETG-ACIS/PCA
24	0.97	HETG-ACIS/PCA
26	0.86	EPIC-pn/PCA
27	0.85	EPIC-pn/PCA
30	0.86	EPIC-pn/PCA
31	0.86	EPIC-pn/PCA
32	0.86	EPIC-pn/PCA

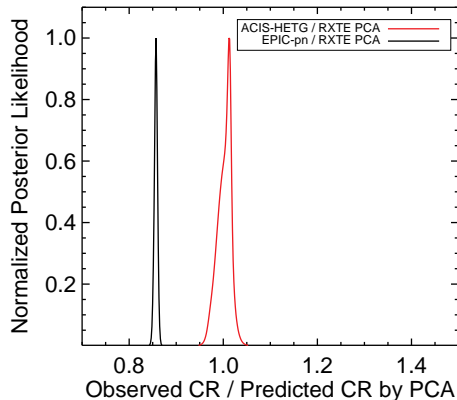


FIG. 13.— Normalized posterior likelihoods of the offsets derived from all ratio measurements for XMM-Newton EPIC-pn/RXTE PCA (black solid lines) and Chandra/RXTE PCA (red solid line).

will change in time. This complication is exacerbated if the calibration source shows intrinsic variability, as is the case with the Crab Nebula, which showed variability at a level of $\approx 7\%$ (Wilson-Hodge et al. 2011). It is, therefore, possible that were we to repeat our cross calibration procedure between RXTE and Chandra at different epochs, we would obtain different offsets. Even though randomly catching an epoch of identical flux measurements between RXTE and Chandra might seem unlikely, we cannot base our conclusions on such a posterior likelihood. For this reason, we now explore the possibility that there is a time-dependent systematic uncertainty in the calibration of the instruments and how this uncertainty would affect the scatter in the measured burst fluxes.

If there were single-epoch measurements of the fluxes during the cooling tails of bursts, this potential systematic error would have to be added to the error budget of the measurements. However, for many of the sources we used for neutron-star radius measurements in Papers I and II, the burst flux measurements were carried over many epochs spanning the lifetime of RXTE. In this case, as we will show below, this potential calibration uncertainty should not be treated as a separate source of systematic uncertainty as it is already inherently part of the measured scatter of observed fluxes.

To demonstrate this point, we compute the mean and the variance of the (burst) flux measured by an instrument (e.g., RXTE/PCA). Let the source flux for each burst be $S_{i,\text{true}}$, with a mean of $\langle S_{i,\text{true}} \rangle = S_{0,\text{true}}$ and an intrinsic dispersion $\sigma_{\text{true}} \neq 0$. Let the instrument have an inferred overall efficiency factor R (e.g., as reported by a calibration team). If this efficiency factor has an unknown systematic bias, which may also be variable in time, then the observed countrate flux will be

$$F_i = (R + B + V_i)S_i, \quad (7)$$

where we have denoted the mean bias in the calibration over the time span of the observations by B and the potential time-variable part by V_i . By definition, $\langle V_i \rangle = 0$.

When an observation is carried out and standard calibration procedures are applied, the observed source flux will be inferred to be equal to

$$S_{i,\text{obs}} = \frac{F_i}{R}, \quad (8)$$

which will be related to the true source flux by

$$S_{i,\text{obs}} = \frac{R + B + V_i}{R} S_{i,\text{true}}. \quad (9)$$

Clearly, the observations reproduce the true source flux if there is no bias in the calibration.

The mean inferred flux of the source is equal to

$$S_0 = \langle S_{i,\text{obs}} \rangle = \left(1 + \frac{B}{R}\right) \langle S_{i,\text{true}} \rangle, \quad (10)$$

where we have used the fact that $\langle V_i S_{i,\text{true}} \rangle = 0$ because the time evolution of the detector response and the variability of the source are uncorrelated. The variance in the inferred burst flux is

$$\begin{aligned} \sigma_{\text{obs}}^2 &= \langle (S_{i,\text{obs}} - S_0)^2 \rangle \\ &= \langle S_{i,\text{obs}}^2 + S_0^2 - 2S_{i,\text{obs}}S_0 \rangle \\ &= \langle S_{i,\text{obs}}^2 \rangle - S_0^2 \end{aligned} \quad (11)$$

and the mean of the square of the inferred fluxes is given by

$$\begin{aligned} \langle S_{i,\text{obs}}^2 \rangle &= \left\langle \left[\left(1 + \frac{B}{R} + \frac{V_i}{R}\right) S_{i,\text{true}} \right]^2 \right\rangle \\ &= \left(1 + \frac{B}{R}\right)^2 \langle S_{i,\text{true}}^2 \rangle + \left\langle \left(\frac{V_i}{R}\right)^2 S_{i,\text{true}}^2 \right\rangle + 2 \left(1 + \frac{B}{R}\right) \left\langle \frac{V_i}{R} S_{i,\text{true}}^2 \right\rangle. \end{aligned} \quad (12)$$

Since $\langle V_i S_{i,\text{true}}^2 \rangle = \langle V_i \rangle \langle S_{i,\text{true}}^2 \rangle = 0$, we find that

$$\begin{aligned} \sigma_{\text{obs}}^2 &= \left(1 + \frac{B}{R}\right)^2 \langle S_{i,\text{true}}^2 \rangle + \left\langle \left(\frac{V_i}{R}\right)^2 S_{i,\text{true}}^2 \right\rangle - \left(1 + \frac{B}{R}\right)^2 \langle S_{i,\text{true}} \rangle^2 \\ &= \left(1 + \frac{B}{R}\right)^2 [\langle S_{i,\text{true}}^2 \rangle - \langle S_{i,\text{true}} \rangle^2] + \frac{1}{R^2} \langle V_i^2 S_{i,\text{true}}^2 \rangle. \end{aligned} \quad (13)$$

The term in the square bracket is equal to the true variance of the source flux $[\langle S_{i,\text{true}}^2 \rangle - \langle S_{i,\text{true}} \rangle^2] = \sigma_{\text{true}}^2$. The average in the second term is $\langle V_i^2 S_{i,\text{true}}^2 \rangle = \sigma_V^2 \langle S_{i,\text{true}}^2 \rangle$, where we have used the definition of the variance of the time-variable bias

$$\sigma_V^2 \equiv \langle V_i^2 \rangle - \langle V_i \rangle^2 = \langle V_i^2 \rangle. \quad (14)$$

As a result,

$$\sigma_{\text{obs}}^2 = \sigma_{\text{true}}^2 \left(1 + \frac{B}{R}\right)^2 + \frac{\sigma_V^2}{R^2} \langle S_{i,\text{true}}^2 \rangle \quad (15)$$

or in terms of fractional errors,

$$\begin{aligned} \left(\frac{\sigma_{\text{obs}}}{S_0}\right)^2 &= \left(\frac{\sigma_{\text{true}}}{\langle S_{i,\text{true}} \rangle}\right)^2 + \frac{\sigma_V^2}{R^2 + B^2} \frac{\langle S_{i,\text{true}}^2 \rangle}{\langle S_{i,\text{true}} \rangle^2} \\ &= \left(\frac{\sigma_{\text{true}}}{\langle S_{i,\text{true}} \rangle}\right)^2 + \frac{\sigma_V^2}{(R + B)^2} \left[1 + \left(\frac{\sigma_{\text{true}}}{\langle S_{i,\text{true}} \rangle}\right)^2\right]. \end{aligned} \quad (16)$$

Keeping only terms up to second order in the dispersions, the final result is

$$\left(\frac{\sigma_{\text{obs}}}{S_0}\right)^2 = \left(\frac{\sigma_{\text{true}}}{\langle S_{i,\text{true}} \rangle}\right)^2 + \frac{\sigma_V^2}{(R + B)^2}. \quad (17)$$

This expression shows that the measured fractional variance in the burst fluxes is equal to the quadrature sum of the intrinsic fractional variance and the fractional variance of the calibration bias. In other words, the observed variance in the burst fluxes is an upper limit to the intrinsic scatter. If the statistical properties of the calibration uncertainties could be measured independently, this contribution could be subtracted from the dispersion of measured fluxes.

6. CONCLUSIONS

In this paper, we quantified the systematic uncertainties that arise from the flux calibration of the X-ray instruments used in neutron star mass and radius measurements. We used simultaneous observations of the burster GS 1826–238 with RXTE/PCA and Chandra HETG/ACIS-S as well as with RXTE/PCA and XMM-Newton/EPIC-pn. We performed a Bayesian statistical analysis to measure the level of offset in the flux calibration between these instruments.

In the case of the comparison between Chandra and RXTE, we found no evidence for a significant offset between the measured fluxes and concluded that the most likely value of the flux ratio is $1.012_{-0.021}^{+0.006}$. As we describe in the appendix, the effect of pileup is unlikely to change the value of this ratio in a statistically significant way. In contrast,

we found a $14.0\pm 0.3\%$ difference between the fluxes inferred using XMM-*Newton*/EPIC-pn and RXTE/PCA. This discrepancy is persistent in all five analyzed bursts and is independent of the source spectrum or countrate.

The flux discrepancy between XMM-*Newton*/EPIC-pn and other detectors has been noted in earlier studies of different sources. Nevalainen et al. (2010) reported a difference between flux measurements with the EPIC-pn, Chandra ACIS (zeroth-order data), and EPIC MOS detectors at a level of 5–10%. According to their results, ACIS flux measurements are significantly higher than EPIC-pn, by $11.0\pm 0.5\%$. Similarly, the difference in the flux measurements between the EPIC-pn and MOS detectors has been noticed earlier (see e.g., Mateos et al. 2009 and XMM-*Newton* calibration documents XMM-*Newton*-SOC-CAL-TN-0018³ and XMM-*Newton*-SOC-CAL-TN-0052⁴); MOS yields fluxes that are approximately 7% higher than EPIC-pn (see also Read et al. 2014). Most recently, using 64 clusters of galaxies, Schellenberger et al. (2014) showed that the effective area cross-calibration uncertainty between ACIS and EPIC-pn is energy dependent and in the 2–7 keV range stabilizes at a 15% level a similar result is also presented by Guainazzi et al. (2015).

Given that the calibration errors of the detectors may be variable in time, it is possible that the excellent agreement between RXTE and Chandra is a coincidence. We showed, however, that even in this case, the spread of the measured burst fluxes reported in Papers I and II already accounts for this potential systematic uncertainty. We, therefore, conclude that, while an overall bias may still exist in the measurements, potential time-dependent flux calibration uncertainties do not increase the error budget of the radius measurements we reported in these earlier papers.

One final consideration is whether the difference in the measured flux between XMM-*Newton* EPIC-pn and the other two instruments also affects the neutron star radii determined through the observations of quiescent low-mass X-ray binaries. The flux levels in question are very different in the observations of these dim sources: they are approximately six orders of magnitude below the peak burst fluxes and the Crab nebula, and about three orders of magnitude below other typical calibration sources (e.g., clusters of galaxies). Given the signal-to-noise ratio of the spectra that is achieved with even the longest observations of quiescent low-mass X-ray binaries, it is not possible to discern any measured flux differences between instruments, even if this difference persisted at the 14% level. This supports the lack of evidence for flux differences presented in the earlier studies (Catuneanu et al. 2013; Heinke et al. 2014; Guillot et al. 2013), which compared neutron star radii derived from the quiescent sources using XMM-*Newton* and Chandra data.

APPENDIX

CORRECTING FOR PILEUP IN CHANDRA HETG/ACIS-S

To account for pileup in the Chandra HETG/ACIS-S spectra, we used a correction that was developed independently by one of the co-authors, Herman Marshall, for mildly piled-up calibration data. The approach relies on the measurement of counts per pixel around the Ir-M and Si-K edges, at which the spectral response changes rapidly. Denoting the observed counts per detector pixel per frame in wavelength bin i as R_i , we define the degradation of the effective area as

$$A'_i = A_i \exp(-aR_i), \quad (\text{A1})$$

where the exponential model was chosen due to the Poisson nature of the probability of multiple events for a given count rate.

The value of the parameter a and the uncertainty associated with its determination was found using an observation of Mk 421 (observation ID 4148) performed on 26–27 October 2002 with the LETGS/ACIS-S for over 91 ks. The data were downloaded from *TGCat*² (Huenemoerder et al. 2011). The countrate spectra were rebinned by a factor of two so that each spectral bin corresponds closely to one ACIS pixel. The source was extremely bright so that there were of order 5000 counts per spectral bin in both the +1 and -1 orders near 2 keV. The count spectrum was divided by the ARF obtained from TGCat to generate spectra in photons/cm²/s/Å for both the +1 and -1 orders. When the two orders are compared (see the top panel of Figure 14) without being corrected for pileup, there are clear edges at Ir-M (6.0 Å) and Si-K (6.74 Å) in the effective-area-corrected spectra. These features arise from differential pileup, where R_i may increase significantly over a few spectral resolution elements at an edge in the effective area of the instrument, causing increased pileup and a larger fractional loss of events with a corresponding decrease in apparent photon flux.

We devised a model-independent method for estimating the parameter a in equation (A1), which depends on the very smooth and slowly varying photon spectrum of Mk 421. Using the ratio of fluxes in the 5.5–5.9 Å range to those in the 6.1–6.5 Å range (straddling the Ir-M edge), we compute the value of a that matches the ratios based on the average R values in the two narrow bands. We find $a = 4.4$ for -1 and $a = 5.5$ for +1 and, therefore, adopt $a = 5$ and a range of acceptable values that are ± 0.5 away from this value. Figure 14 shows the sensitivity of the spectral inversion to a ; for $a = 4$, the spectra still show edges, while, for $a = 7$, the data are over-corrected to form an excess over a smooth spectral model. (A global spectral fit to a double power law indicates that the photon spectrum should drop monotonically by only 1% per Å through this wavelength range, so the assumption that the fluxes are equal should be good to 1%.)

³ <http://xmm2.esac.esa.int/docs/documents/CAL-TN-0018.pdf>

⁴ <http://xmm2.esac.esa.int/docs/documents/CAL-TN-0052.ps.gz>

² <http://tgcate.mit.edu>

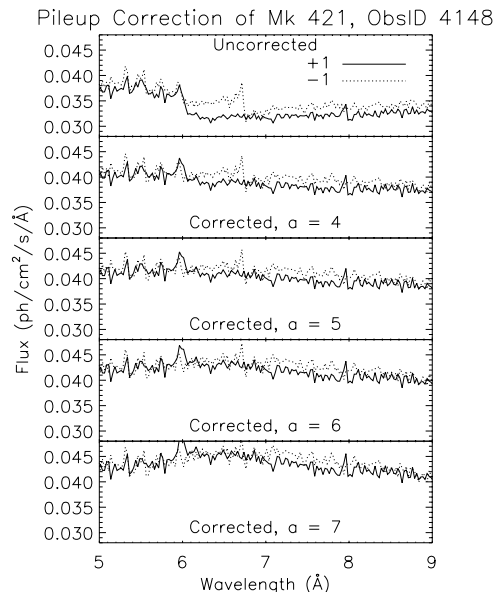


FIG. 14.— The 5–9 Å region of the unfolded photon spectra of Mk 421 (ObsID 4148), taken with the *Chandra* LETG/ACIS-S. The top panel shows the original data, uncorrected for pileup, as obtained from the *tgcat* archive of *Chandra* grating spectra. The remaining panels show how the spectra appear after adjusting the effective area according to equation (A1), for several values of the parameter a . It is clear that the uncorrected spectra show spectral jumps at the instrumental Ir-M (6.0 Å) and Si-K (6.74 Å) edges. The spectra are most consistent with a simple smooth power law for $a = 5$.

Using equation (A1), which is verified to $R_i = 0.05$ cts/frame/pixel, a $\pm 10\%$ uncertainty in a results in at most a $\pm 2.5\%$ uncertainty in A'_i/A_i , which is smaller than the expected calibration uncertainty in A_i . This method required the HRMA effective area correction implemented in 2005, which corrected the Ir-M edge caused by a thin contaminant layer on the HRMA. Note that, the correction given in equation (A1) is valid for low to modest pileup, i.e., $R_i < 0.2$ cts/frame/pixel and the data used to compute the coefficient a ranged up to about 0.10 cts/s/pixel. This yields a maximum correction of about 50%.

In our comparison between RXTE and *Chandra*, we took into account the pileup losses in the predicted countrates rather than correcting the observed rates for pileup. If we denote by y_i the number of photons per detector pixel per frame that should have been recorded in wavelength bin i in the absence of pileup, we can then invert the above expression to obtain

$$R_i = y_i [0.63 \exp(-6y_i) + 0.37], \quad (\text{A2})$$

This approximation is appropriate for $y_i < 0.065$ cts/frame/pix. The burst spectra reached 0.08 cts/frame/pix, which is a small extrapolation from the domain for which the correction was derived.

We thank the members of both the *Chandra* and XMM-Newton help desks for their help and suggestions throughout this study. We also thank Tod Strohmayer for his encouragement to pursue a study of flux calibration uncertainties in neutron star radius measurements. We thank Keith Jahoda for illuminating discussions on the calibration of the RXTE/PCA instrument. TG was supported by Scientific Research Project Coordination Unit of Istanbul University. Project numbers: 49429, 57321 and 48934. DP and FO gratefully acknowledge support from NASA ADAP grant NNX12AE10G and NSF grant AST-1108753 for this work. This research has made use of data obtained from the High Energy Astrophysics Science Archive Research Center (HEASARC), provided by NASA's Goddard Space Flight Center.

REFERENCES

- Arnaud, K. A. 1996, in *Astronomical Society of the Pacific Conference Series*, Vol. 101, *Astronomical Data Analysis Software and Systems V*, ed. G. H. Jacoby & J. Barnes, 17–4
- Becker, R. H., Pravdo, S. H., Serlemitsos, P. J., Swank, J. H., & Hoffman, J. 1976, *IAU Circ.*, 2953, 1
- Catuneanu, A., Heinke, C. O., Sivakoff, G. R., Ho, W. C. G., & Servillat, M. 2013, *ApJ*, 764, 145
- Cornelisse, R., et al. 2003, *A&A*, 405, 1033
- Damen, E., Magnier, E., Lewin, W. H. G., et al. 1990, *A&A*, 237, 103
- Demorest, P. B., Pennucci, T., Ransom, S. M., Roberts, M. S. E., & Hessels, J. W. T. 2010, *Nature*, 467, 1081
- Galloway, D. K., Cumming, A., Kuulkers, E., Bildsten, L., Chakrabarty, D., & Rothschild, R. E. 2004, *ApJ*, 601, 466

- Galloway, D. K., Munro, M. P., Hartman, J. M., Psaltis, D., & Chakrabarty, D. 2008, *ApJS*, 179, 36
- Guainazzi M., David, L., Grant, C.E., Miller, E., Natalucci, L., Nevalainen, J., Petre, R., Audard, M., 2015, *J. Astron. Telesc. Instrum. Syst.* *1*(4), 047001
- Guillot, S., Servillat, M., Webb, N. A., & Rutledge, R. E. 2013, *ApJ*, 772, 7
- Güver, T., Psaltis, D., Özel, F. 2012a, *ApJ*, 747, 76, Paper I
- Güver, T., Özel, F., & Psaltis, D. 2012b, *ApJ*, 747, 77, Paper II
- Heinke, C. O., Cohn, H. N., Lugger, P. M., et al. 2014, *MNRAS*, 444, 443
- Houck, J. C., & Denicola, L. A. 2000, in *Astronomical Society of the Pacific Conference Series*, Vol. 216, *Astronomical Data Analysis Software and Systems IX*, ed. N. Manset, C. Veillet, & D. Crabtree, 591–+
- Huenemoerder, D. P., Mitschang, A., Dewey, D., et al. 2011, *AJ*, 141, 129
- Jahoda, K., Markwardt, C. B., Radeva, Y., et al. 2006, *ApJS*, 163, 401
- Kirsch, M. G., Briel, U. G., Burrows, D., et al. 2005, *Proc. SPIE*, 5898, 22
- Lattimer, J. M., & Prakash, M. 2001, *ApJ*, 550, 426
- Lodders, K. 2003, *ApJ*, 591, 1220
- Lewin, W. H. G., van Paradijs, J., & Taam, R. E. 1993, *Space Sci. Rev.*, 62, 223
- Makino, F. 1988, *IAU Circ.*, 4653, 2
- Markert, T. H., Canizares, C. R., Clark, G. W., et al. 1977, *ApJ*, 218, 801
- Mateos, S., Saxton, R. D., Read, A. M., & Sembay, S. 2009, *A&A*, 496, 879
- Nevalainen, J., David, L., & Guainazzi, M. 2010, *A&A*, 523, A22
- Noergaard-Nielsen, H. U., Budtz-Joergensen, C., Westergaard, N. J., & Schnopper, H. W. 1994, *A&A*, 285, 705
- Özel, F. 2006, *Nature*, 441, 1115
- Özel, F., & Psaltis, D. 2009, *Phys. Rev. D*, 80, 103003
- Özel, F., Güver, T., & Psaltis, D. 2009, *ApJ*, 693, 1775
- Pinto, C., Kaastra, J. S., Costantini, E., & Verbunt, F. 2010, *A&A*, 521, A79
- Read, J. S., Markakis, C., Shibata, M., et al. 2009, *Phys. Rev. D*, 79, 124033
- Read, A. M., Guainazzi, M., & Sembay, S. 2014, *A&A*, 564, A75
- Schellenberger, G., Reiprich, T. H., Lovisari, L., Nevalainen, J., & David, L. 2014, arXiv:1404.7130
- Sembay, S., Guainazzi, M., Plucinsky, P., & Nevalainen, J. 2010, *X-ray Astronomy 2009; Present Status, Multi-Wavelength Approach and Future Perspectives*, 1248, 593
- Shaposhnikov, N., Jahoda, K., Markwardt, C., Swank, J., & Strohmayer, T. 2012, *ApJ*, 757, 159
- Stairs, I. H. 2006, *Journal of Physics G Nuclear Physics*, 32, 259
- Swank, J. H., Becker, R. H., Boldt, E. A., et al. 1977, *ApJ*, 212, L73
- Tanaka, Y. 1989, *Two Topics in X-Ray Astronomy, Volume 1: X Ray Binaries. Volume 2: AGN and the X Ray Background*, 296, 3
- Toor, A., & Seward, F. D. 1974, *AJ*, 79, 995
- Ubertini, P., et al. 1997, *IAU Circ.*, 6611, 1
- van Paradijs, J. 1979, *ApJ*, 234, 609
- van Paradijs, J. 1978, *Nature*, 274, 650
- Weisskopf, M. C., Guainazzi, M., Jahoda, K., et al. 2010, *ApJ*, 713, 912
- Wilson-Hodge, C. A., Cherry, M. L., Case, G. L., et al. 2011, *ApJ*, 727, L40